2D Layered Perovskites

Solution Processable Materials

The recent discovery that single-layer 2D perovskites can be prepared using solution processing techniques[1] has been followed by enormous research into optoelectronic applications of 2D perovskites including light emitting diodes (LEDs),[2] phototransistors,[3] and solar cells.[4]

Tunable Emission Wavelength

Photoluminescent 2D perovskites have an emission wavelength that changes depending on the layer thickness and the choice of amine and halide. We offer an excellent portfolio of the most popular 2D perovskite compositions for photoluminescence based devices.

Improved Moisture Stability

Solar cells fabricated with 2D perovskites have improved stability in moist air compared to 3D perovskites.[4]

Formula	Cat. No.	Layer Thickness	$(RNH_3)_2(MeNH_3)_{n-1} Pb_n X_{3n+1}$		
			R	X	n
$(BA)_2PbI_4$	910961	n=1	Bu	I	1
$(BA)_2PbBr_4$	910953	n=1	Bu	Br	1
$(PEA)_2PbI_4$	910937	n=1	PE	I	1
$(PEA)_2PbBr_4$	910945	n=1	PE	Br	1
$(BA)_2(MA)Pb_2I_7$	912816	n=2	Bu	I	2
$(BA)_2(MA)_2Pb_3I_{10}$	912557	n=3	Bu	I	3
$(BA)_2(MA)_3Pb_4I_{13}$	914363	n=4	Bu	I	4
$(BA)_2(MA)_4Pb_5I_{16}$	912301	n=5	Bu	I	5

BA = n-butylammonium; PEA = 2-phenylethylammonium;
MA =methylammonium, Bu=n-butyl, PE=2-phenylethyl

References:

1) Dou, L.; Wong, A. B.; Yu, Y.; Lai, M.; Kornienko, N.; Eaton, S. W.; Fu, A.; Bischak, C. G.; Ma, J.; Ding, T.; Ginsberg, N. S.; Wang, L-W.; Alivisatos, A. P.; Yang, P. *Science* **2015**, *349,* 1518. DOI: 10.1126/science.aac7660

2) Yuan, M.; Quan, L. N.; Comin, R.; Walters, G.; Sabatini, R.; Voznyy, O.; Hoogland, S.; Zhao, Y.; Beauregard,E. M.; Kanjanaboos, P.; Lu, Z.; Kim, D. H.; Sargent, E. H. *Nat. Nanotechnol.* **2016**, *11,* 872. DOI: 10.1038/NNANO.2016.110

3) Shao, Y.; Liu, Y.; Chen, X.; Chen, C.; Sarpkaya, I.; Chen, Z.; Fang, Y.; Kong, J.; Watanabe, K.;Taniguchi, T.; Taylor, A.; Huang, J.; Xia, F. *Nano Lett.* **2017**, *17,* 7330. DOI: 10.1021/acs.nanolett.7b02980

4) Cao, D. H.; Stoumpos, C. C.; Farha, O. K.; Hupp, J. T.; Kanatzidis, M. G. *J. Am. Chem.* Soc. **2015**, *137,* 7843. DOI: 10.1021/jacs.5b03796

SigmaAldrich.com/perovskite

The Life Science business of Merck operates as MilliporeSigma in the U.S. and Canada.

Sigma-Aldrich®

Lab & Production Materials

Boosting Photoelectrochemical Ethanol Evolution on Reduced Graphene Oxide Functionalized Photocathode

Mi Jung, Chang Woo Kim, So Yeon Kim, Amol U. Pawar, Don Keun Lee, and Young Soo Kang*

Herein, a reduced graphene oxide (rGO) functionalized photocathode is studied for selective production of solar liquid fuels depending on dark and solar light illumination condition. rGO functionalized photocathode with p–n junction at the core–shell interface of ZnO@ZnTe is prepared with a three-step synthetic process. Preparation of ZnO nanorod, formation of ZnTe on ZnO nanorod by anion-exchange and then, finally, rGO layers are functionalized on the surface of ZnO@ZnTe photocathode. The photoelectrochemical (PEC) system of $BiVO_4 \| KHCO_3 \| ZnO@ZnTe@rGO$ combination is introduced for selective solar liquid fuel production by CO_2 reduction reaction (CO2RR). Functionalization of rGO layers on photocathode enables the multi-electron shuttling function for the enhanced charge transfer efficiency due to its large charge capacitance, which results in producing liquid fuels such as HCHO and EtOH selectively as solar liquid fuels. These results in this work clearly demonstrate a possibility of solar liquid fuel product selectivity by PEC CO2RR.

1. Introduction

Ever-increasing the concentration of atmospheric carbon dioxide leads to a disastrous environmental change by global warming, which can be solved by converting CO_2 into solar liquid fuels or useful chemicals through extensive research as exploring energy resources.[1,2] Discovering new technology for converting CO_2 into solar liquid fuels as eco-friendly energy resources aims to accomplish a new energy paradigm with carbon-free or carbon neutrality.[3] Carbon-free or carbon neutrality energy system and their utilization are recognized as

alternative one such as solar, wind, electric energy, etc. to carbon-based resources.[4] Carbon-free energy system powered by alternative one is a clear mean to relieve the concentration of CO_2 in atmosphere. Together with carbon-free energy, carbon upcycling is a series of CO_2 capture, storage, and conversion for the utilization and is aimed to the production of energy source with high energy density and reducing CO_2 emission. In this energy sector, the direct utilization of CO_2 as a one of the major conversions into high density solar liquid fuels has received a great interest in terms of net-carbon zero emission.[5]

Artificial photosynthesis provides a ground-breaking path to produce carbon-neutral fuels in the process of conversion to value-added chemicals from thermodynamically stable CO_2 feedstock.[6] Such series of multi-proton-assisted sequential multi-electron catalytic reaction have been suggested as a keystone on a production of wide range of hydrocarbon compounds.[7] For the past decades, preliminary studies have been reported on CO_2 reduction reaction (CO2RR) to valuable energetic chemicals like formic acid (HCOOH), formaldehyde (HCHO), and alcohols (MeOH, EtOH) via photocatalytic (PC), electrochemical (EC), photoelectrochemical (PEC), and bioelectrochemical approaches.[8] Pioneering research on artificial photosynthesis has left scientific remarks on the point of thermodynamically favorable pathway and fast kinetics.[6,9–13] Evolved products have been expected to rely on thermodynamics and kinetics parameters at the rate determining step. Low catalytic performances suffer from the low current density, high overpotential, large onset potential, which could be determined with linear sweep voltammetry (LSV) curve and Tafel slope. It also consequently results in the low conversion efficiency, faradaic efficiency, and turnover frequency.[14] Nevertheless, the low product selectivity of CO2RR has also been limited due to unclearness on the CO2RR mechanism and other parameter tuning for the thermodynamics and kinetics.[15]

To address the product selectivity of CO2RR, 2-dimensional (2-D) atomic arrangement with sp^2 hybridization in graphene have been rapidly explored for catalytic performance in energy application.[14,16–18] Carbon honeycombed lattice results in an intrinsically favorable clues for carrier mobility, conductivity, band energy, surface area, etc. However, pristine graphene owns unfavorable catalytic performances for CO2RR because

M. Jung, S. Y. Kim
Department of Chemistry
Sogang University
Seoul 121-742, Republic of Korea
C. W. Kim
Department of Nanotechnology Engineering
Pukyong National University
Busan 48513, Republic of Korea
A. U. Pawar, D. K. Lee, Y. S. Kang
Environmental & Climate Technology
Korea Institute of Energy Technology (KENTECH)
Naju, Jeollanamdo 58217, Republic of Korea
E-mail: yskang@kentech.ac.kr

**ADVANCED
SCIENCE NEWS**

www.advancedsciencenews.com

**ADVANCED
ENERGY
MATERIALS**

www.advenergymat.de

of their neutral carbon atoms.[14] The needs of catalytic performances drive to introduce the functionalization into pristine graphene by adding hetero atoms and manipulation of defects. The rational design of graphene derivatives has been expected to be ideal candidate for the enhanced catalytic performance of CO2RR in the theoretical and experimental reports.[19–21] Boron-assisted charge polarization,[22] Ag-attributed binding energy,[23] defect engineering,[24] surface tuning[25] on graphene have been achieved as efficient strategies for the enhancement of CO2RR efficiency. Together with intrinsic properties from graphene, reduced graphene oxide plays a key role to electron acceptor and transporter in the view of electrochemical aspect due to large charge capacity and good conductivity, controllable defect sites to induce dipole on the surface for providing adsorption site and affinity to CO_2 molecules. Especially, given that reduced graphene oxide (rGO) is exposed to solar light, electron–hole is efficiently separated and results in favorable functions of PEC CO2RR on the surface of electrode.

In our previous work, we investigated a high electrical conductivity and charge trapping behavior induced by rGO and resulting in the easy electron capturing and sequential multi-electron transfer for photocatalytic CO2RR.[26] After that, a product selectivity for solar liquid fuels of PEC or PC CO2RR depends on energy level tuned rGO structure.[27] More recently, rGO layer in dark cathode provide multi-electron accumulation and sequential multi-electron transfer into CO2RR site for solar liquid fuel production of PEC or PC CO2RR.[28] Our findings suggest that the product selectivity depends on the several parameters for the CO2RR process such as sequential multiple number of electron and proton transfer ability, tuning CO_2 reduction potential (energy), optimizing rGO structure for the reduction energy tuning of the sequential multi-electron transfer into CO2RR site for product selectivity. The CO_2 conversion efficiency into solar liquid fuels is also depending on the cathode function with lower activation energy of the rate

determining step of the first step electron transfer reaction for the formation of CO_2 anion radical intermediates ($CO_2^{-\bullet}$) and fast charge transfer between electron donor rGO and CO2RR site through interface.

In the present work, we demonstrate the product selectivity between HCHO and C_2H_5OH as a solar liquid fuel by PEC CO2RR in the comprehensive system of photoanode and photocathode. Our concern on the product selectivity between C1 and C2 products places the stability of intermediates with the different lifetime of it in addition to the previous parameters and favorable charge transfer kinetics for CO2RR. To prove our viewpoints, herein, rGO functionalized ZnO@ZnTe as a photocathode and $BiVO_4$ photoanode (BVO) are suggested for developing PEC CO2RR systems with the desired product selectivity and efficiency.
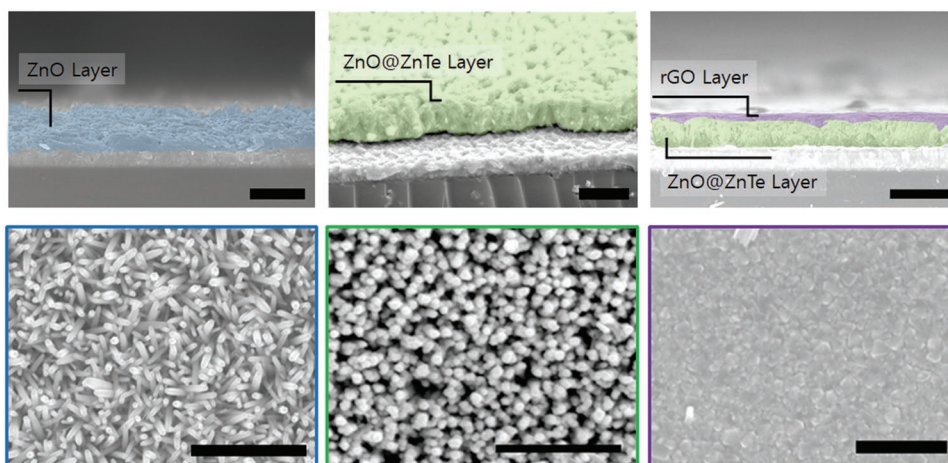
2. Result and Discussion

To achieve the goal, rGO was functionalized on the surface of ZnO@ZnTe cathode as core@shell heterostructures. Approach of rGO functionalized photocathode by layer-by-layer approach for PEC CO2RR was illustrated in **Scheme 1**. rGO functionalized ZnO@ZnTe electrode were prepared with a three-step approach. 1-Dimensional (1-D) ZnO nanorods were vertically grown from ZnO seed layer on FTO substrates by hydrothermal reaction.[29] The surface of the ZnO nanorods was converted to ZnTe by an anion exchange reaction. Te^{2-} was adsorbed on the ZnO nanorods and diffused into the nanorods by substituting the O atoms due to the lower solubility product constant at the growth process.[30] Finally, rGO layer was loaded on the surface of ZnO@ZnTe nanorod arrays by thermal reduction of graphene oxide. Field emission scanning electron microscope (FE-SEM, **Figure 1**) shows the cross-sectional and top-viewed FE-SEM images of ZnO nanorod (blue), ZnO@ZnTe nanorod
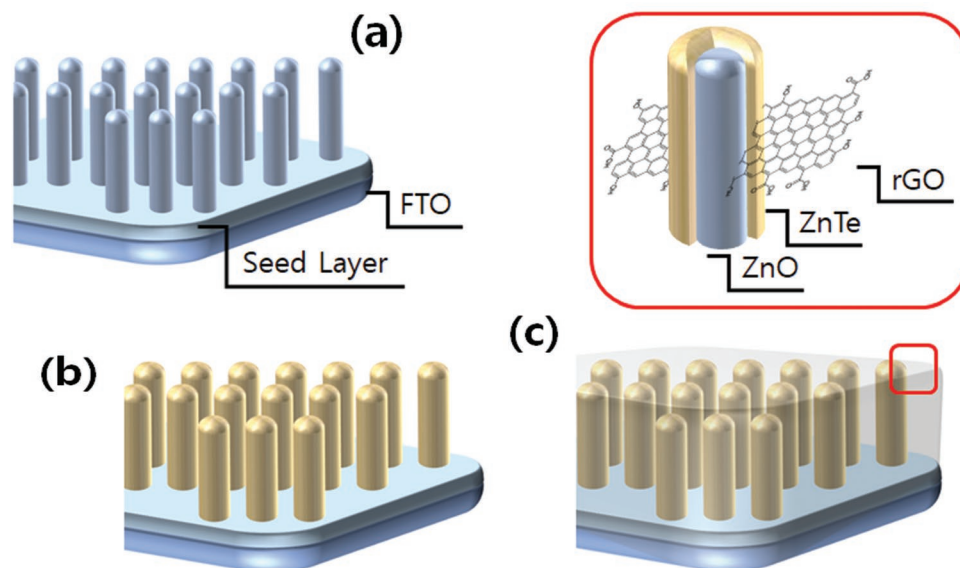
Scheme 1. Illustration of rGO functionalized photocathode by layer-by-layer coating for photochemical CO_2 reduction. a) Hydrothermally synthesized ZnO rod, b) the formation of ZnTe shell on ZnO rod, and c) rGO functionalized electrode.

**ADVANCED
SCIENCE NEWS**

www.advancedsciencenews.com

**ADVANCED
ENERGY
MATERIALS**

www.advenergymat.de

Figure 1. Cross-sectional and top viewed scanning electron microscopic images of ZnO nanorod (blue), ZnO@ZnTe nanorod (green), and rGO functionalized ZnO@ZnTe film (violet) prepared by layered by layered formation, respectively. Black bars in the images correspond 2 μm.

(green), and rGO functionalized ZnO@ZnTe film (violet) prepared by layer-by-layer formation. FE-SEM images show that ZnO nanorods were grown on the ZnO seed layer. ZnTe nanorods have a rough surface in their own outer morphology. After GO solution was spin-coated on ZnO@ZnTe nanorods and GO-loaded ZnO@ZnTe nanorod sample was reduced under the reductive gas flowing, rGO layer was formed. It

indicates that rGO was homogeneously covered on the surface of ZnO@ZnTe nanorods.

For better observation of as-prepared nanorod, an individual rod of each film was characterized with energy-filtered transmission electron microscope (EFTEM) in **Figure 2**. A typical image of ZnO@ZnTe shows that each layer of interface is obviously distinguishable as a core@shell. With comparison of oxygen
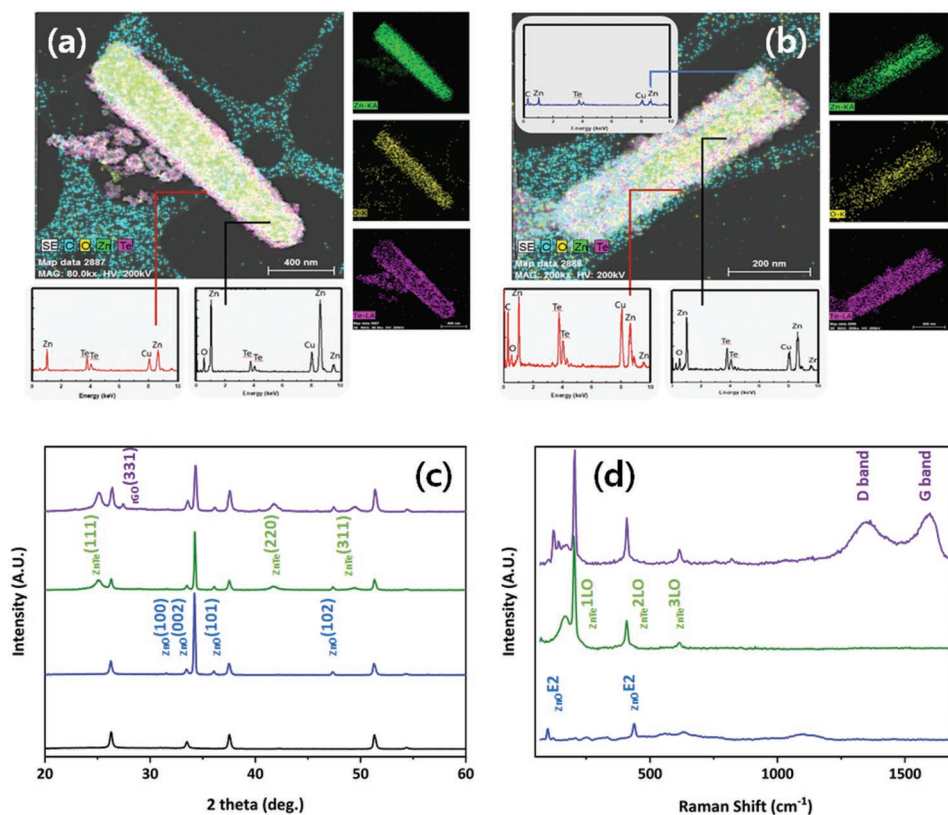
Figure 2. Elemental mapping images of a) ZnO@ZnTe nanorod and b) rGO functionalized ZnO@ZnTe film. c) XRD patterns and d) Raman spectra of FTO (black), ZnO (blue), ZnO@ZnTe (green), and rGO functionalized ZnO@ZnTe thin film (violet) prepared by layer by layer coating, respectively.

**ADVANCED
SCIENCE NEWS**

www.advancedsciencenews.com

**ADVANCED
ENERGY
MATERIALS**

www.advenergymat.de

among mapping element between core and shell, the amount of oxygen in the part of core is larger than that in the part of shell. XPS characteristic peaks at 1021.08 and 1021.58 eV were assigned as Zn^{2+} 2p in ZnO and ZnO@ZnTe nanorod, respectively (Figure S1, Supporting Information). The core level XPS spectrum of Te 3d shows that peaks at binding energy of 572.4 and 582.8 eV corresponds to Te^{2+} from ZnTe. Both peaks at binding energy of 576 and 586 eV are attributed to Te^{4+} from TeO_2 resulting from superficial oxidation.[31] It indicates that Te^{2+} ion is absorbed and replaced with oxygen in ZnO lattice, resulting in the formation of ZnTe as a shell. To figure out the existence of rGO, top-most layer in rGO functionalized ZnO@ZnTe nanorod was selected and observed in detail. As expected, the larger amount of carbon was detected in outer layer than that of inner core region in rGO functionalized ZnO@ZnTe nanorod. The comparison of both samples shows that rGO was homogeneously coated on individual ZnO@ZnTe nanorod.

For proving the crystal structure, typical 3 kinds of samples, ZnO (blue), ZnO@ZnTe (green), and rGO functionalized ZnO@ZnTe film (violet) were investigated by XRD and Raman spectroscopy. From the result of ZnO nanorod, representative peaks detected at 31.769°, 34.421°, 36.252°, and 47.538° are corresponding to (100), (002), (101), and (102) planes, respectively, and it is matched as hexagonal wurtzite phase of ZnO (JCPDS#36-1451).[32] In the samples treated by anion exchange reaction, three peaks at 25.32°, 41.805°, and 49.496° were additionally detected and matched well with (111), (220), and (311) planes of cubic phase of ZnTe (JCPDS#15-0746).[33] Two characteristic peaks appeared at 25.1° and 27.38° in rGO functionalized samples are corresponding to the (002) and (331) plane of rGO.[34]

Such tendency of layered structures appeared in the comparison of Raman spectra in the typical 3 kinds of samples. In as-synthesized ZnO nanorod, the peaks at 98 and 437 cm^{-1} are dominantly detected and assigned to E_2 (low) and E_2 (high) modes, respectively.[35] E_2 (low) is associated with the vibration of oxygen atom and E_2 (high) is corresponding to heavy Zn sublattices. There are two dominant peaks at around 205 and 410.2 cm^{-1} in the anion exchange treated sample. As the symmetric peaks of ZnTe, the peak at 410 cm^{-1} were assigned to first-order longitudinal optical (LO) and second-order (2LO) overtone phonon scattering of ZnTe crystal structure, respectively.[30] Small additional peaks are observed in the spectral range of 120–150 cm^{-1}, which is ascribed to the existence of Te^{2-}-rich phases from ZnTe. Together with characteristic peaks of ZnO and ZnTe, G band at 1589.5 cm^{-1} and D band of sp^3 carbon at 1352 cm^{-1} were additionally detected. It means that G band and D band come from the sp^2 and sp^3 carbon in rGO lattice, respectively. Based on the results of XRD and Raman spectrum, rGO layer was well covered on ZnO@ZnTe as core@ shell structure.

To figure out the role of rGO layer on PEC CO2RR, ZnO@ ZnTe, and rGO functionalized ZnO@ZnTe were mounted as a cathode in PEC CO2RR reactor with CO_2 gas purged $KHCO_3$ aqueous solution during the illumination of BVO photoanode. Electrochemical performance between ZnO@ZnTe (black) and rGO functionalized ZnO@ZnTe film (red) was compared under dark and one sun solar light illumination (**Figure 3**). Cyclic voltammograms (CV) have been compared between ZnO@ZnTe and ZnO@ZnTe@rGO with and without incident light in the potential range 0 to −1 V versus Ag/AgCl with scan rate 20 mV S^{-1}. ZnO@ZnTe electrode produced 0.5 mA of cathodic current at 1.0 V in cyclic voltammograms. The ZnO@ZnTe electrode shows that the current value increases in cathodic compartment due to ZnTe absorbs more visible light and generates more free electrons which contribute for enhancing the current. Interestingly, cathodic current increased to 0.9 mA in rGO functionalized electrode under dark condition. Especially cathodic current was strictly increased at −0.55 V compared with −0.6 V in the ZnO@ ZnTe electrode. Under the one sun solar light illumination, ZnO@ZnTe produced the increased cathodic current of 0.74 and 1.1 mA with rGO functionalized electrode. The difference of cathodic current between dark and one sun solar light illumination condition come from high photon absorption ability and suppression of charge recombination of heterostructure in ZnO@ZnTe electrode. CV behavior of rGO electrode provided that rGO affected on the enhanced cathodic current not only due to large charge capacitance for better charge accumulation ability mainly, but also have a minor effect by higher photon absorption ability. Such electrochemical behavior with positively shifting of cathodic current indicates that the existence of rGO in electrode enhances catalytic reactivity of CO2RR. The larger charge capacitance of rGO functionalized cathode allows effective charge accumulation on the rGO layer of the cathode and favorable electron transfer to CO_2 molecules and results in a lower overpotential for fast charge transfer through the interface. Tafel slopes in rGO functionalized ZnO@ZnTe and ZnO@ZnTe cathodes were obtained and slopes were calculated to be −220 and −414 mV dec^{-1}, respectively. It is clearly proved that rGO functionalized ZnO@ZnTe cathode has larger charge transfer coefficient than that of ZnO@ZnTe electrode, indicating a decreased overpotential barrier for charge transfer of the cathode surface for CO2RR. For understanding the influence of rGO to the conductivity and charge transfer efficiency through the interface between photocathode and electrolyte, Nyquist plot of electrochemical impedance spectroscopy (EIS) was monitored in the frequency range between 0.1 and 105 Hz at −0.8 V. EIS result of ZnO@ZnTe electrode without ($\bigcirc$, unfilled circle) and with CO_2 ($\bullet$, filled circle) under −0.6, −0.7, and −0.8 V (Figure S2, Supporting Information). Regarding this point, Nyquist plot shows that the charge transfer at the interface between rGO cathodes and electrolyte is more favorable than ZnO@ZnTe cathode because the impedance as energy barrier for charge transfer is markedly reduced due to large charge capacity and excellent charge trapping ability of rGO (Figure 3d). The surface modified ZnO@ZnTe photocathode with rGO layer enhanced the flow of the electron transfer for CO_2 reduction reaction through the interface between ZnO@ZnTe@rGO and CO_2 molecules adsorbed on the rGO layer of the cathode in the electrolyte. Equivalent circuit diagram and values of resistance and capacitance obtained by fitting EIS spectra of ZnO@ ZnTe@rGO electrode in presence of light and CO_2 was recorded in Figure S3 (Supporting Information).

To prove the enhancement of charge transfer from the effect of rGO functional layer, time-resolved photoluminescence (TRPL) and incident photon to current efficiency (IPCE) of ZnO (blue), ZnO@ZnTe (green), and rGO functionalized
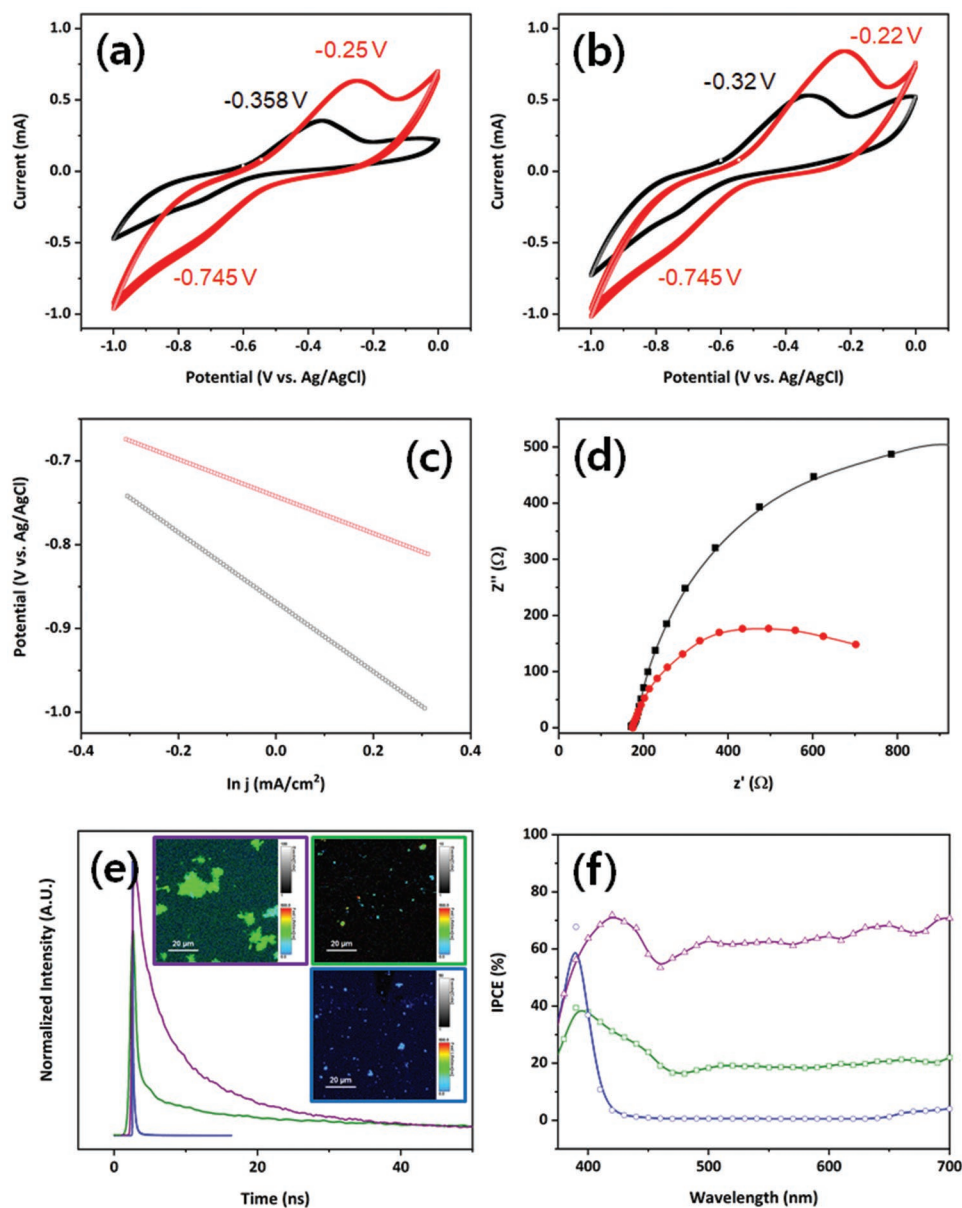
Figure 3. a) CV curves under dark and b) under illumination, c) Tafel-plots and d) Nyquist plots of ZnO@ZnTe (black) and rGO functionalized ZnO@ZnTe thin film (red). e) Time-resolved photoluminescence and f) incident photon to current efficiency in ZnO (blue), ZnO@ZnTe (green), and rGO functionalized ZnO@ZnTe (violet), respectively.

ZnO@ZnTe (violet) were determined, respectively. The inserted images in Figure 3e show the 2D TRPL images of ZnO electrode (blue), ZnO@ZnTe electrode (green), and rGO functionalized electrode (violet).

In TR-PL images, the part covered with green indicates larger number of excited electrons and the part covered with black color image indicates less number of excited electrons. Average life-times are monitored by fitting the PL decay using multi-exponential curves (Table S1, Supporting Information). Compared that ZnO nanorod electrode show the average lifetimes of the charge carriers of 47 ns, the average lifetimes of the charge carriers of ZnTe decorated ZnO nanorods film was calculated to be 286 ns. The increased decay time attributes to effective

charge separation/transfer process in the p–n junctioned interface of ZnO@ZnTe. Interestingly, the average decay time of the rGO functionalized ZnO@ZnTe nanorods film was remarkably reduced to 0.36 ns. As an electron scavenger with high charge capacity and mobility, rGO layers facilitate to extract electron from the surface of ZnO@ZnTe and acts as a charge transfer mediator.[26,36] It confirmed the electron transfer from the conduction band of ZnTe to the rGO layer and effective suppression of electron/hole pair recombination. Each layer depending on the decay time was investigated with IPCE spectra of ZnO, ZnO@ZnTe, and rGO functionalized ZnO@ZnTe electrode as shown in Figure 3f. As-prepared ZnO nanorod show IPCE of 70% at 390 nm because of their UV responsive absorber. In ZnO@ZnTe
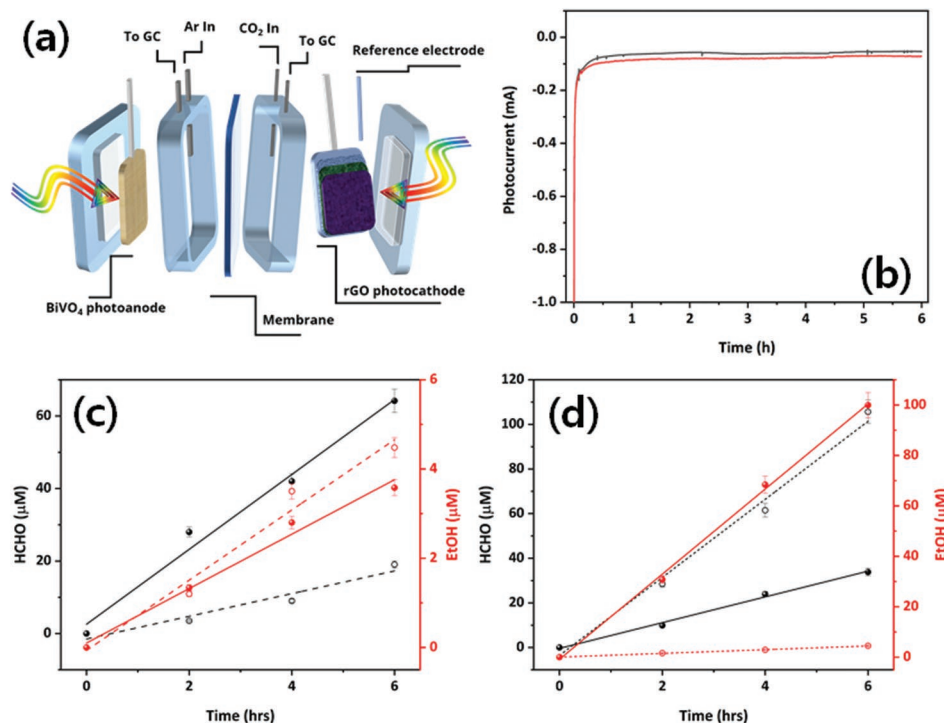
Figure 4. a) Schematic illustration of CO_2 reduction reactor using photoanode and photocathode. b) I–t curve of ZnO@ZnTe photocathode (black) and rGO photocathode (red) under illumination. GC spectra of c) ZnO@ZnTe photocathode and d) rGO photocathode. Illuminated anode only (black) and both electrode (red).

cathode, IPCE was recorded to 73% was observed in ZnO@ZnTe photocathode. The highest IPCE was recorded to ≈40% in rGO functionalized electrode. Based on the result on charge transfer from TRPL and IPCE, it is concluded that electrons can be captured in the rGO functional layers from p–n junctioned ZnO@ZnTe electrode and transported to CO_2 molecules adsorbed on rGO layer for CO2RR to produce solar liquid fuels more easily.

To understand the effect of rGO functional layer for photocatalytic performances in CO2RR, current density of ZnO@ZnTe cathode and rGO functionalized ZnO@ZnTe photocathodes were comparatively determined. Our CO_2 reduction reactor have a compartment of BiVO$_4$ photoanode‖photocathode in a CO_2-purged 0.5 m of KHCO$_3$ electrolyte and one sun solar light was illuminated to just anode and both photoelectrodes, respectively (**Figure 4**). Based on chopped linear sweep voltammetry (LSV) curves (Figure S4, Supporting Information), I–t curves for ZnO@ZnTe photocathode and rGO functionalized ZnO@ZnTe photocathode measured at −0.8 V versus Ag/AgCl under one sun solar light illumination for 6 h. A cathodic photocurrent density was observed as 0.065 mA in ZnO@ZnTe photocathode under illumination. rGO functionalized photocathode produced a slightly reduced cathodic photocurrent density as 0.085 mA under illumination. Figure 4b shows that the photo-generated electron was transported from ZnO@ZnTe photocathode to rGO functional layer and circuits were stable. rGO functional layer can accumulate multi-electrons on the rGO layer of the cathode more efficiently than ZnO@ZnTe cathode considering stability and durability. It indicates that the electron transport from conduction band of rGO layer coated on the surface of

ZnO@ZnTe electrode can allow a sequential multi-electron shuttling function into CO_2 molecules adsorbed on rGO layer to produce solar liquid fuels. Such tendency was identified with strong electron delocalization cloud in TRPL images as shown in Figure 3. After CO2RR at −0.8 V under the illumination, solar liquid fuel products were identified and quantified with GC. In our CO2RR system, EtOH and formaldehyde were detected at retention times of 6.9 and 7.6 min, respectively. Notably, the GC spectrum at designated retention time was not present in the N$_2$-bubbling experiment. As following the calibration curves of EtOH and HCHO, quantification of each CO2RR product is performed. With applied bias potential of −0.8 V for PEC CO2RR under one sun solar light illumination on photoanode, ZnO@ZnTe electrode produced HCHO of 19.04 μm and EtOH of 4.48 μm for 6 h reaction, respectively. With one sun solar light illumination of both electrodes, ZnO@ZnTe photocathode produced HCHO production of 64.19 μm as a major product in Figure 4c. Interestingly rGO functionalized cathode produced HCHO production of 108.64 μm as a major product, of which larger amount of HCHO was observed than pristine ZnO@ZnTe cathode in Figure 4d. Compared with the products obtained by ZnO@ZnTe cathode, rGO functional layer is more proper to form HCHO as a dark cathode. Interestingly ethanol was strictly increased after CO2RR under one sun solar light illumination on both electrode in Figure 4d. Produced HCHO was relatively reduced but EtOH was produced to 99.94 μm as a major product. It is presumed that sequential multi-electron shuttling function due to large charge capacity from rGO functional layer in the dark cathode allows the evolution of HCHO to EtOH. The detailed reaction mechanism for HCHO

and EtOH have been presented in Figure S5 (Supporting Information).[27,28] Faradic efficiency and solar to chemical efficiency calculation between ZnO@ZnTe and ZnO@ZnTe@rGO electrodes with different light illumination region was recorded in Table S2 (Supporting Information). Considering products in dark cathode and photocathode, it is clear that more easy charge transfer was evolved under one sun solar light illumination on rGO functional layer to produce EtOH requiring larger number of electrons. Together with intrinsic CO_2 adsorption ability, rGO functional layer with larger charge capacity induces to accumulate multi-electrons and facilitate sequential multi-electron shuttling for CO_2 reduction into liquid fuels.

With our observation in the configuration of BVO∥rGO functionalized cathode, product selectivity between HCHO and EtOH was suggested. As the electrochemical reduction process, rGO functional layer facilitates sequential multi-electron transfer to adsorbed CO_2 on the surface of rGO layer on the cathode with applied potential, leading formation of CO_2 radical anion radical ($CO_2^{-\bullet}$) as rate determining step. With the help of protons in catholyte, CO_2 anion radical evolves to CHO radicals as a key intermediate for HCHO formation. Under the one sun solar light illumination condition, photon-induced excited electron from ZnO@ZnTe photocathode is transported to rGO functional layer, in which it facilitates large amount of adsorbed CHO radical intermediate. Relatively proton deficient condition leads to the longer life-time of CHO radical intermediate for the C–C dimerization for production of ethanol. The lower solar liquid fuel product concentration of PEC CO2RR with one sun solar light irradiation on both photoanode and photocathode compared to only on photoanode and dark cathode can be caused by the re-oxidation of products by produced hole in the cathode surface.

3. Conclusion

In summary, rGO functionalized ZnO@ZnTe p–n junctioned photocathode was prepared with a three-step synthetic process for PEC CO2RR. Functionalization of rGO layers on ZnO@ZnTe photocathode increased their charge transfer efficiency due to the large charge capacitance and charge trapping ability. By applying $BiVO_4$ photoanode under one sun solar light illumination, rGO functionalized dark cathode produced HCHO as a major product in the CO2RR. With one sun solar light illumination on rGO functionalized ZnO@ZnTe photocathode, the increased EtOH was selectively evolved. rGO functional layer under one sun solar light illumination condition contributed to enhance the evolution of EtOH by multi-electron shuttling function of rGO layer for CO2RR, at the same time, due to lower proton density, which leads to the longer life-time of CHO radical intermediate for the C–C dimerization for production of ethanol. These results presented in this work clearly demonstrate a possibility of product selectivity for the solar liquid fuels by CO2RR.

4. Experimental Section

Materials: Zinc acetate dihydrate ($Zn(CH_3COO)_2 \cdot 2H_2O$, ≥98%), zinc nitrate hexa-hydrate ($Zn(NO_3)_2 \cdot 6H_2O$, ≥99%), hexamethylenetetramine ($C_6H_{12}N_4$, ≥99%), sodium borohydride ($NaBH_4$ ≥ 98%), 1-methyl-2-pyrrolidinone (C_5H_9NO, 99.5%), sodium tellurite (Na_2TeO_3,

100 mesh, 99%) and potassium bicarbonate ($KHCO_3$, 99.7%) were purchased from Sigma-Aldrich. All chemicals were used without further treatment.

Fabrication of Photocathode and Photoanode: Fluorine doped tin oxide (FTO) substrate (2 cm × 2.2 cm) was cleaned by sonication in a mixture solution of 2-propanol, acetone and water (1:1:1, v/v/v). A solution for ZnO seeds was prepared by dissolving zinc acetate of 0.02 g in 20 mL of ethanol. A ZnO seed solution was spin-coated on FTO by a speed of 2000 rpm for 30 s and repeated four times. And then, spin-coated FTO was heat-treated at 450 °C for 30 min in air. ZnO seed layered FTO was immersed into in a mixed solution of 10 mL of zinc nitrate aqueous solution (0.1 M) and 10 mL of hexamethylenetetramine aqueous solution (0.1 M). The solution was heated to 90 °C for 4 h in the Teflon-lined autoclave. After reaction, samples were cleaned with DI water and ethanol with several times and then, heat-treated at 300 °C for 2 h in air. For the formation of ZnTe, 0.1 g of sodium tellurite and 1 g of sodium borohydride were dissolved in 100 mL of deionized water and then stirred for 12 h. The solution color was changed to black, transparent purple and transparent white sequentially. ZnO nanorod was immersed into sodium tellurite solution and maintained at 95 °C for 2 h for an anion ion exchange reaction. The ZnO@ZnTe nanorod film was cleaned with deionized water and ethanol with several times and then heat-treated at 350 °C for 2 h under Ar flowing. GO (graphene oxide Nano powder, US research Nanomaterials, Inc.) dispersed in NMP solution (N-methyl-2-pyrrolidinone, Sigma). The GO solutions (1 mg mL^{-1}) were spin-coated on the ZnO@ZnTe nanorod at 500 rpm for 1 min, and followed by thermal reduction at 150 °C for 30 min under Ar/H_2 (95/5, v/v) gas flowing. (040)-facet controlled $BiVO_4$ photoanode was prepared by a seed-layer approach.

Characterization of Materials: The morphology of the samples was characterized with field emission scanning electron microscope (FESEM, JEOL, JSM7600F) which was operated by 20 kV of incident electron beam energy. Transmission electron microscope (TEM, JEOL JEM-2100 F operating at 200 kV) were performed to characterize individual ZnO and ZnO@ZnTe nanorod which were scraped from the films, dispersed in ethanol, and dropped on the TEM grid (Ted Pella, lacey carbon type-A 300 mesh, copper, #01890-F). The crystal structure of the samples was determined using an X-ray diffractometer (XRD, Rigaku miniFlex-II desktop X-ray diffractometer, Cu K_α radiation, λ = 0.154 056 nm), operated by 40 kV and 40 mA. X-ray photoelectron spectroscope (XPS, K-alpha, Thermo UK) analysis was performed with a monochrometer Al Ka X-ray source and calibrated by the binding energy of C1s 284.6 eV.

PEC Characterization: All of the PEC experiments were carried out in a quartz three-electrode cell which is consisted of two separated compartments of anode and cathode with Nafion-117 membrane. An external bias potential of −0.8 V (vs Ag/AgCl in 3.0 M KCl) was applied under 1-sun (AM 1.5 G, 100 mW cm^{-2}) solar light illumination during the CO_2 reduction. Cyclic voltammetry (CV) and chronoamperometry (CA) were performed using a potentiostat PL-9 (PhysioLab Co., Ltd., Korea) instruments. Electrochemical impedance spectrum (EIS) Nyquist plots for ZnO@ZnTe and rGO functionalized ZnO@ZnTe electrodes was measured using PL-9 electrochemical workstation with a magnitude of the modulation signal of −0.8 V, ranging from 105 to 0.1 Hz.

For the incident photon to electron conversion efficiency (IPCE, HS Technologies, Korea) measurement, the absolute intensity of the monochromic incident light was referenced by a silicon photodiode (model BS-500, Bunkoukeiki Co. Ltd., Japan). Time-resolved photoluminescence (TR-PL) measurement was carried out using a confocal microscope (MicroTime-200, Picoquant, Germany) with a 40× objective. The life-time measurements were performed at the Korea Basic Science Institute (KBSI, Daegu Center, Korea). A single-mode pulsed diode laser (375 nm with 30 ps pulse width and 1–10 μW power) was used as an excitation source. A dichroic mirror (Z375RDC, AHF), a long-pass filter (HQ405lp, AHF), a 75 μm pinhole, and an avalanche photodiode detector (PDM series, MPD) were used to collect emission photons from the samples. The acquisition time of each pixel was 1 ms. Exponential fitting for the obtained PL decays was accomplished using the Symphotime-64 software (Ver. 2.2). Steady-state PL spectra were measured by dividing and guiding the PL signal through an optical fiber to the external spectrometer (F-7000, Hitachi).

PEC CO$_2$ Reduction: A PEC reactor consisted of transparent quartz glass was assembled with two compartments separated by a Nafion-117 membrane. (040)-BVO and Ag/AgCl electrodes were used as the photoanode and reference electrode, respectively. rGO functionalized ZnO@ZnTe film and KHCO$_3$ electrolyte in the cathodic compartment was trygon-tubed to GC for monitoring the products. After CO$_2$ was purged into 100 mL of 0.5 M of KHCO$_3$ aqueous solution for 45 min, 20 mL of the solution was used as an electrolyte of each part. During PEC CO2RR, CO$_2$ was purged continuously into the cathodic compartment with the constant flow rate of 20 sccm rate, and one sun solar light was simultaneously illuminated to BiVO$_4$ photoanode or both BiVO$_4$ and the cathode with a 300-W Xe Lamp (HAL-320, Ashai spectra, Japan).

Qualitative and quantitative analysis of CO$_2$ reduction products were done with gas chromatography 7890B series of GC-FID (Agilent Technologies) equipped with a DB-624 column (60 m $\times$ 250 μm $\times$ 1.4 μm) and Stratum Purge & Trap (TELEDYNE TEKMAR) was also used for the analysis of CO$_2$ reduction products. The calibration curves were obtained by using each standard solution of formaldehyde and ethanol. Formaldehyde and ethanol were observed at 7.6 and 6.9 min, respectively. The concentration was calculated by comparing the peak area relative to the peak area of the standard solution in the calibration curves.

Supporting Information

Supporting Information is available from the Wiley Online Library or from the author.

Conflict of Interest

The authors declare no conflict of interest.

Data Availability Statement

The data that support the findings of this study are available from the corresponding author upon reasonable request.

[1] S. Navarro-Jaén, M. Virginie, J. Bonin, M. Robert, R. Wojcieszak, A. Y. Khodakov, *Nat. Rev. Chem.* **2021**, *5*, 564.

[2] W. Lai, Z. Ma, J. Zhang, Y. Yuan, Y. Qiao, H. Huang, *Adv. Funct. Mater.* **2022**, *32*, 2111193.

[3] S. J. Dhoble, B. Vengadaesvaran, N. T. Kalyani, A. K. Arof, *Energy Materials: Fundamentals to Applications*, Elsevier Ltd., Netherlands **2021**.

[4] R. Eisenberg, H. B. Gray, G. W. Crabtree, *Proc. Natl. Acad. Sci. USA* **2020**, *117*, 12543.

[5] S. J. Davis, N. S. Lewis, M. Shaner, S. Aggarwal, D. Arent, I. L. Azevedo, S. M. Benson, T. Bradley, J. Brouwer, Y.-M. Chiang, C. T. M. Clack, A. Cohen, S. Doig, J. Edmonds, P. Fennell, C. B. Field, B. Hannegan, B.-M. Hodge, M. I. Hoffert, E. Ingersoll, P. Jaramillo, K. S. Lackner, K. J. Mach, M. Mastrandrea, J. Ogden, P. F. Peterson, D. L. Sanchez, D. Sperling, J. Stagner, J. E. Trancik, et al., *Science* **2018**, *360*, 9793.

[6] T. Wang, J. Gong, *Nat. Energy* **2020**, *5*, 642.

[7] A. Kumar, V. Hasija, A. Sudhaik, P. Raizada, Q. Van Le, P. Singh, T.-H. Pham, T. Kim, S. Ghotekar, V.-H. Nguyen, *Chem. Eng. J.* **2022**, *430*, 133031.

[8] S. C. Peter, *ACS Energy Lett.* **2018**, *3*, 1557.

[9] H. Huang, H. Song, J. Kou, C. Lu, J. Ye, *J. Energy Chem.* **2022**, *67*, 309.

[10] Ya Liu, L. Guo, *J. Chem. Phys.* **2020**, *152*, 100901.

[11] X. Zhang, S.-X. Guo, K. A. Gandionco, A. M. Bond, J. Zhang, *Mater. Today Adv.* **2020**, *7*, 100074.

[12] T. Banerjee, F. Podjaski, J. Kröger, B. P. Biswal, B. V. Lotsch, *Nat. Rev. Mater.* **2021**, *6*, 168.

[13] Md. D. Hossain, Y. Huang, T. H. Yu, W. A. Goddard Iii, Z. Luo, *Nat. Commun.* **2020**, *11*, 2256.

[14] A. Hasani, M. A. Teklagne, H. H. Do, S. H. Hong, Q. Van Le, S. H. Ahn, S. Y. Kim, *Carbon Energy* **2020**, *2*, 158.

[15] L. Fan, C. Xia, F. Yang, J. Wang, H. Wang, Y. Lu, *Sci. Adv.* **2020**, *6*, 3111.

[16] T. Tsujiguchi, Y. Kawabe, S. Jeong, T. Ohto, S. Kukunuri, H. Kuramochi, Y. Takahashi, T. Nishiuchi, H. Masuda, M. Wakisaka, K. Hu, G. Elumalai, J.-I. Fujita, Y. Ito, *ACS Catal.* **2021**, *11*, 3310.

[17] Z. Sun, Y. H. Hu, *Acc. Mater. Res.* **2021**, *2*, 48.

[18] Z. Yang, C. Yang, J. Han, W. Zhao, S. Shao, S. Li, H. Gao, H. Xie, X. Zhang, *J. Mater. Chem. A* **2021**, *9*, 19681.

[19] S. Ozden, L. Delafontaine, T. Asset, S. Guo, K. A. Filsinger, R. D. Priestley, P. Atanassov, C. B. Arnold, *J. Catal.* **2021**, *404*, 512.

[20] T. Zhang, W. Li, K. Huang, H. Guo, Z. Li, Y. Fang, R. M. Yadav, V. Shanov, P. M. Ajayan, L. Wang, C. Lian, J. Wu, *Nat. Commun.* **2021**, *12*, 5265.

[21] C. Hu, Q. Dai, L. Dai, *Cell Rep. Phys. Sci.* **2021**, *2*, 100328.

[22] N. Sreekanth, M. A. Nazrulla, T. V. Vineesh, K. Sailaja, K. L. Phani, *Chem. Commun.* **2015**, *51*, 16061.

[23] K. Lv, Y. Fan, Y. Zhu, Yi Yuan, J. Wang, Y. Zhu, Q. Zhang, *J. Mater. Chem. A* **2018**, *6*, 5025.

[24] P. Han, X. Yu, Di Yuan, M. Kuang, Y. Wang, A. M. Al-Enizi, G. Zheng, *J. Colloid Interface Sci.* **2019**, *534*, 332.

[25] Z. Sun, T. Ma, H. Tao, Q. Fan, B. Han, *Chem* **2017**, *3*, 560.

[26] H. R. Park, A. U. Pawar, U. Pal, T. Zhang, Y. S. Kang, *Nano Energy* **2021**, *79*, 105483.

[27] M. J. Kang, C. W. Kim, H. G. Cha, A. U. Pawar, Y. S. Kang, *Appl. Catal., B* **2021**, *295*, 120267.

[28] A. U. Pawar, U. Pal, J. Y. Zheng, C. W. Kim, Y. S. Kang, *Appl. Catal., B* **2022**, *303*, 120921.

[29] T. K. Van, L. Q. Pham, D. Y. Kim, J. Y. Zheng, D. Kim, A. U. Pawar, Y. S. Kang, *ChemSusChem* **2014**, *7*, 3505.

[30] S. Luo, X. He, H. Shen, J. Li, X. Yin, D. Oron, H. Lin, *RSC Adv.* **2017**, *7*, 14837.

[31] Y. J. Zhang, J-W. Jang, J. Lee, J. H. Kim, H. Kumagai, J. Lee, T. Minegishi, J. Kubota, K. Domen, J. Lee, *Energy Environ. Sci.* **2015**, *8*, 3597.

[32] A. U. Pawar, C. W. Kim, M. J. Kang, Y. S. Kang, *Nano Energy* **2016**, *20*, 156.

[33] M. Iqbal, Y. Wang, H. Hu, M. He, A. H. Shah, P. Li, L. Lin, A. R. Woldu, T. He, *Electrochim. Acta* **2018**, *272*, 203.

[34] X. Jiao, Y. Qiu, L. Zhang, X. Zhang, *RSC Adv.* **2017**, *7*, 52337.

[35] B. Koo, S. Byun, S.-W. Nam, S.-Y. Moon, S. Kim, J. Y. Park, B. T. Ahn, B. Shin, *Adv. Funct. Mater.* **2018**, *28*, 1705136.

[36] P. Xu, S. Huang, M. Liu, Y. Lv, Z. Wang, J. Long, W. Zhang, H. Fan, *Catalysts* **2019**, *187*, 187.